Journal of
Ceramic Science
and Technology

J. Ceram. Sci. Tech., **03** [03] 119-130 (2012)
DOI: 10.4416/JCST2012-00004
available online at: http://www.ceramic-science.com

Gadolinia-Neodymia-Co-Stabilized Zirconia Materials with High Toughness and Strength

F. Kern*

Institut für Fertigungstechnologie keramischer Bauteile, Universität Stuttgart, (Institute for Manufacturing Technologies of Ceramic Components and Composites, University of Stuttgart), 70569 Stuttgart, Allmandring 7b, Germany
received January 23, 2012; received in revised form May 24, 2012; accepted June 28, 2012

Abstract

Tetragonal zirconia polycrystals (TZP) ceramics are frequently used in structural applications owing to their attractive mechanical properties. The established standard materials Y-TZP and Ce-TZP suffer from deficiencies in either toughness or strength.

Combining different stabilizer oxides can be a feasible strategy to obtain TZP materials with both high strength and toughness. 1 mol% gadolinium oxide-2 mol% neodymium oxide co-stabilized zirconia powder (GdNd2-TZP) was produced from pyrogenic unstabilized zirconia nanopowder via the nitrate route and blended with 0.5 and 20 vol% alumina respectively. Materials hot-pressed at 1200 – 1350 °C were characterized in respect of mechanical properties, microstructure and phase composition. GdNd2-TZP combines very high fracture resistance with a 4-pt-bending strength > 1000 MPa. The alumina-toughened zirconia (ATZ) composite reaches higher strength at slightly lower toughness. ATZ exhibits higher hardness and less sensitivity to variations in processing conditions. Under optimized sintering, both materials exhibit an extremely high threshold stress intensity K_0 of up to 6 – 7.5 MPa·√m. X-ray diffraction results show that the materials tend to decompose with rising sintering temperatures as a result of progressive formation of cubic phase and monoclinic zirconia.

Keywords: Zirconia, mechanical properties, R-curve, phase composition, microstructure

I. Introduction

Structural ceramics consisting of partially stabilized zirconia can achieve high strength and toughness at ambient application temperature. The excellent mechanical properties are caused by transformation toughening, an effect based on the martensitic-stress-induced transformation of the metastable tetragonal to the stable monoclinic phase. This phase transformation is associated with volume expansion and shear. The transformed zone forming in the wake of a proceeding crack slows or inhibits further crack propagation [1]. The partial stabilization of the tetragonal phase is commonly achieved with the addition of metal oxides such as magnesia, calcia, yttria and ceria. Calcia and magnesia are used to produce PSZ (partially stabilized zirconia)-type ceramics with nanometric lenticular precipitates in a coarse cubic matrix. TZP (tetragonal zirconia polycrystals) ceramics such as Ce-TZP and Y-TZP consist of small tetragonal grains [2].

Ce-TZP has high toughness but low strength and requires sintering in an oxidizing atmosphere to avoid reduction of CeO_2 to Ce_2O_3. Transformation can be autocatalytic and thus affects large volumes [3]. Y-TZP stabilized with 2.5 – 3.5 mol% yttria has high strength but only moderate toughness, the transformation zone in Y-TZP is considerably smaller [4]. Crystallographic details of martensitic transformations in different zirconia alloys are summarized by Kelly [1]. TZP powders can be produced by means of two methods. The most frequently used procedure for Y-TZP is co-precipitation of zirconia and stabilizer oxide, which leads to homogeneous dopant distribution at atomic level [5]. A coating process that deposits the stabilizer oxide on the surface of monoclinic zirconia grains can be performed either with wet chemical processes or intensive milling [6, 7, 8].

It has been demonstrated by various authors that Y-TZP from the coating process can achieve higher toughness and is less prone to low-temperature degradation, an effect to be considered especially in case of biomedical implants [9]. The coating process is very versatile for the production of TZP powders with different dopants and dopant concentrations. Co-stabilization of TZP by means of coating has been reported for e.g. Y-Yb-TZP, Y-Gd-TZP, Y-Nd-TZP and Y-Ce-TZP [10 – 12]. Co-stabilization can lead to tailored properties – either mechanical or functional – for a variety of applications. Phase diagrams (zirconia and one stabilizer oxide) are available in good quality for the most common systems. An excellent overview of RE_2O_3-ZrO_2 systems (RE = La, Nd, Sm, Gd, Dy and Yb) is given by Wang [13]. According to these latest data on Nd_2O_3-ZrO_2, the tetragonal field in the temperature range covered in this study is very narrow, the t/t+c phase bound-

* Corresponding author: frank.kern@ifkb.uni-stuttgart.de

ary at 1500 K is found at ~1–1.2 mol% Nd_2O_3. A further complication arises from the fact that the cubic field on the stabilizer-rich side extends down to only ~1480 K. During further cooling, first a t+ pyrochlore field extending from 1326–1480 K follows. There is thus evidence that neither phase relations given by Andrievskaya for ZrO_2-Nd_2O_3 claiming the absence of cubic phase nor the data by Rouanet claiming the absence of pyrochlore are correct [14,15]. For the quasi-ternary systems (zirconia and two different stabilizing oxides), only a few systems are well described. The fluorite structure in Nd_2O_3-Y_2O_3-ZrO_2 has been studied by Hinatsu, a calculated tentative phase diagram for the zirconia-rich corner of the same system has been published by Vleugels [16,12].

The latter diagram does not seem to represent the thermodynamic relation correctly as the t/t+c phase boundary in the system ZrO_2-Nd_2O_3 is claimed at 4.3 % Nd_2O_3 at 1450 °C, which is in sharp contrast to Wang's findings (~1 mol%).

Lakiza has calculated phase relations in the system Gd_2O_3-Al_2O_3-ZrO_2 [17]. The gadolinia zirconia system shows a "regular" behaviour like yttria-zirconia, the t+c field is, however, wider, the t/t+c boundary at 1500 K is found at ~1.2 mol%, the t+c/c boundary at this temperature is at 8.5 mol% Gd_2O_3 [13]. No data are available for the Gd_2O_3-Nd_2O_3-ZrO_2 system. Owing to the only slightly higher ionic radius of Gd^{3+} compared to Y^{3+} similar behaviour of the ternary composites can be expected. The group of Vleugels and Van der Biest have introduced Y-Nd-TZP ceramics with high toughness and applied these ceramics in EDM-machinable TZP composites [12,18,19]. Gadow has shown that alumina-toughened zirconia (ATZ) materials from 1.5Y-1.5Nd-co-doped TZP possess high strength and toughness [20]. A detailed study of fracture mechanics in TZP co-doped with two trivalent lanthanides has, however, never been published. The correct determination of fracture toughness of zirconia-toughened materials with high toughness is, however, very challenging. Indentation methods using direct crack length measurements are often used owing to their convenience. Quinn and Bradt have argued that the Vickers indentation procedure does not exactly measure a crack propagation parameter as a "crack arrest process occurs in the presence of a multiple-cracked material environment and in a highly complex residual stress condition" [21]. In the case of zirconia, there is probably no problem of multicracking, the residual stress situation, however, seems even more complicated owing to transformation-derived stress. Residual strength measurements of zirconia using a pre-notched specimen are also very sensitive to sample preparation [22]. Annealing procedures to remove residual stresses must be avoided for oxygen-deficient hot-pressed materials as they would change the composition and degree of stabilization. This present paper on GdNd2-TZP is the first in a series about the manufacturing and characterization of lanthanide oxide co-doped TZP for structural applications.

II. Experimental Procedure

A pyrogenic unstabilized zirconia nanopowder VP-Ph (Evonik, Germany) with a crystallite size d_c of 12 nm and a specific surface area S_{BET} of 40 m²/g was coated with gadolinia and neodymia. The unstabilized zirconia still contains some tetragonal phase owing to fast quenching in the production process [8]. The coating process was conducted following the nitrate route introduced by Yuan and further refined to the requirements of the ultrafine starting powders [6,23]. Nitrate solutions for coating were obtained by dissolving Nd_2O_3 and Gd_2O_3 (both Chempur, Germany, 99.9 % purity) in boiling 5N nitric acid. The stabilizer concentration in the TZP was set to 1 mol% gadolinia and 2 mol% neodymia. The coated powder was blended with 0.5 vol% for the TZP feedstock and 20 vol% α-alumina APA0.5 (Ceralox, USA, d_{50} = 300 nm, S_{BET} = 8 m²/g) for ATZ by means of milling with 3Y-TZP balls in 2-propanol for 4 h. The oven-dried (85 °C/12 h) and screened (100 μm) powders were then ready for processing. In the following, the 0.5 vol% alumina-doped material is called TZP, the composite containing 20 vol% alumina is called ATZ.

Hot pressing (KCE, Germany) was conducted in a rectangular (22 x 42 mm²) boron-nitride-clad graphite mould in vacuum at 1200–1400 °C for TZP and 1250–1350 °C for ATZ. The sintering temperature was varied in 50 K increments. Heating to final temperature was conducted at 50 K/min to 1150 °C. Then a load of 30 MPa was applied, after a dwell of 10 min, heating to final temperature was continued at 15 K/min. The load was increased to 60 MPa for 1-h dwell. Cooling was conducted in the press in argon atmosphere. Two disks of each parameter combination were produced. The TZP disks sintered at 1400 °C were cracked, all other samples were macroscopically intact.

The resulting hot-pressed disks were lapped with 15-μm diamond suspension and polished to a 1-μm finish with diamond suspension. The samples were cut into bars of 4 mm in width with a diamond wheel (Struers Accutom, Germany). Sides and edges were ground with a 40-μm diamond disk and bevelled by polishing with 15-μm diamond suspension. 14 bars were available for mechanical testing. Remaining pieces were kept for XRD and hardness testing. The dimensions of the bending bars after the complete machining process were (L x W x H) 22 x 3.7 ± 0.1 x 1.7 ± 0.1 mm³.

The bending strength σ_{4pt} was measured in a 4-pt setup with 20 mm outer and 10 mm inner span (Zwick, Germany) on ten samples, the crosshead speed was 2.5 mm/min to avoid subcritical crack growth. Vickers hardness measurements of HV10 (Bareiss, Germany, five indents each) and HV0.1 (Fischer, Germany, twelve indents each) were conducted. The indentation modulus E_{IND} was calculated from the loading-unloading curve of the HV0.1 measurement. The indentation fracture resistance was determined by means of direct crack length measurement of five HV10 indents and calculated according to Anstis' model [24]. Indentation strength in bending ISB according to Chantikul was measured in the same 4-pt setup on three bending bars pre-damaged with a HV10 indent in the middle of the tensile side, the crosshead speed was 2.5 mm/min [25]. Residual strength tests and crack length measurements were made immediately after indentation. In or-

der to obtain information on R-curve behaviour, stable indentation cracks were grown in flexure tests according to the procedure shown by Dransmann and refined by Benzaid [26,27]. Four HV10 indents placed in 1.5-mm distance with the diagonals parallel and perpendicular to the sides of a bending bar were made. As recommended by Benzaid, the bar was left to rest for two days so that the cracks were able to grow subcritically to a stable extension, then the development of crack length with increasing load was measured, loading was performed at 5 mm/min without dwell. The loading stages were defined in respect of the maximum residual strength values in the ISB test, typically the first loading was performed at one third of the maximum strength and increased in 50 – 100 MPa increments. During post-indentation bending, an indentation crack is subjected to a total stress intensity factor K_{tot}, given as the sum of the residual indentation stress intensity factor, K_{res}, and the applied bending contribution, K_a:

$$K_{tot} = K_{res} + K_a = \chi \cdot P \cdot c^{-1.5} + \psi \cdot \sigma \cdot c^{0.5} \quad (1)$$

where c and ψ are, respectively, the residual stress and crack geometry coefficients ($\psi = 1.27$ for the chosen geometry); σ is the applied bending stress and c is the surface crack length. Plotting $\psi \cdot \sigma \cdot c^{0.5}$ versus $P \cdot c^{-1.5}$ allows determination of K_{IC} as the extrapolated ordinate intercept of a straight line with the slope χ. $K_{app,0}$ is the stress intensity factor at the kink of the curve. The threshold toughness K_0 can be calculated as the difference between K_{IC} and $K_{App,0}$ [27]. According to Lube, reading of χ from the slope is only a rough estimation and only strictly valid for materials without R-curve behaviour [28]. Moreover, it has to be considered in materials with R-curve behaviour, there is no fixed level of K_{IC} as K_R rises with crack extension. Therefore as K_{IND} and K_{ISB} are measured at different crack extensions, different fracture resistance values are obtained with $K_{ISB} > K_{IND}$.

The microstructure of the composites was investigated by means of SEM (Zeiss, Germany) at low acceleration voltage of 3 kV on carbon-coated thermally etched (1200 °C/30 min air) polished surfaces. Chemical composition in different regions of the microstructure was investigated by means of EDX (energy-dispersive X-ray analysis) (Leo, UK). The phase composition of polished surfaces and fracture faces was investigated with X-ray diffraction (XRD) in the 2θ-range between 27° and 33°. The peak areas of the monoclinic (-111) and (111) as well as the tetragonal (101) reflex was numerically integrated and the volume fractions of the monoclinic phase was calculated using the calibration curve of Toraya [29]. The density was determined based on the Archimedes principle in water.

III. Results

(1) Microstructure

The microstructure of TZP and ATZ sintered at 1250 and 1350 °C are shown in Figs. 1 – 4. In both materials a bimodal grain size distribution of TZP is observed. Larger grains are embedded in a very fine-grained matrix. The fine matrix grains grow from 60 – 150 nm at 1250 °C to 150 – 250 nm at 1350 °C. The larger grains grow from 300 – 500 nm to 500 – 1000 nm. The large grains may be isolated or arranged in larger groups. Images of lower magnification reveal that the fraction of large grains in TZP is in the range of ~ 10 area%. Alumina addition does not completely prevent this bimodal structure in TZP, the amount of large grains is, however, lower (~ 5 area%). The grains in the TZP matrix of ATZ are slightly smaller than in TZP at low sintering temperatures. At 1350 °C, no grain refinement by alumina can be observed. The alumina grains are well dispersed and retain their original grain size.

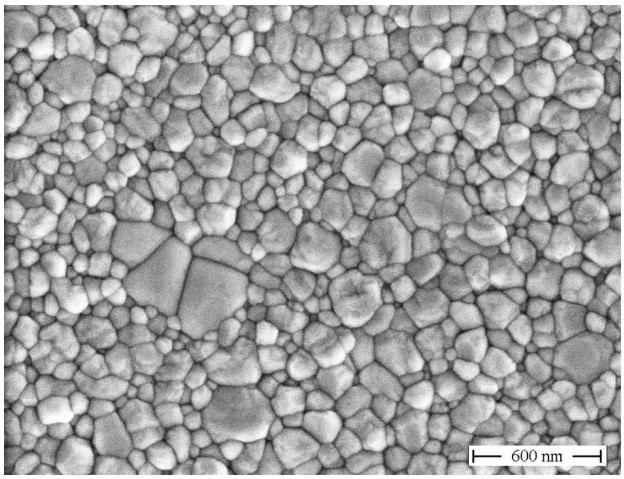

Fig. 1: SEM image, microstructure of TZP sintered at 1250 °C/1 h.

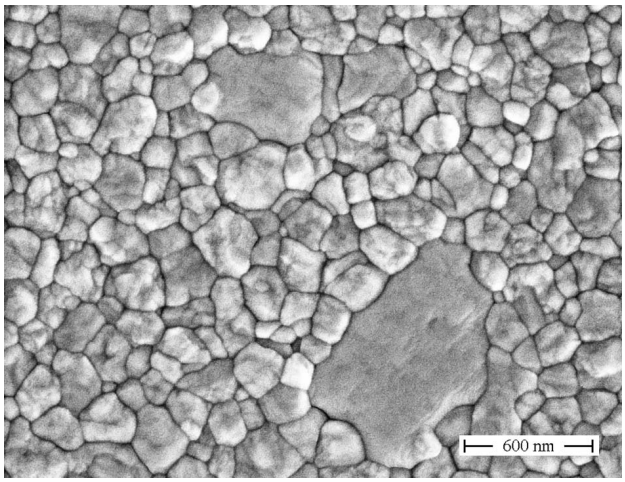

Fig. 2: SEM image, microstructure of TZP sintered at 1350 °C/1 h.

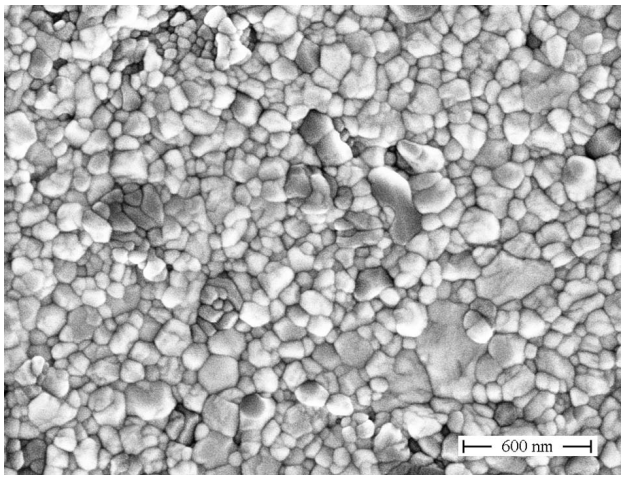

Fig. 3: SEM image, microstructure of ATZ sintered at 1250 °C/1 h.

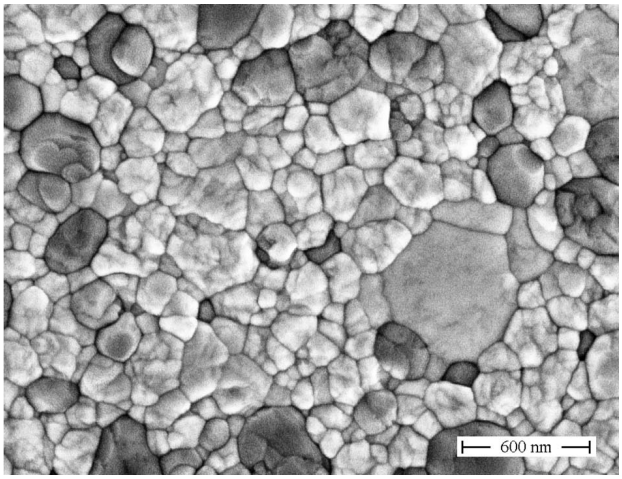

Fig. 4: SEM image, microstructure of ATZ sintered at 1350 °C/1 h.

In order to determine the chemical composition of the coarse grains and the fine grain matrix, an EDX analysis was conducted. In TZP materials sintered at 1250 °C and 1350 °C the concentration of zirconia, neodymia and gadolinia was measured in assemblies of larger grains and in the fine grain matrix. Results show for both sintering temperatures that the concentration of stabilizers in the large grains is significantly higher than in the matrix. Results for TZP sintered at 1250 °C are summarized in Table 1. The molar ratio between Nd_2O_3 and Gd_2O_3 in the large grains is 2.5:1, in the matrix the ratio is 1.9:1. Measured values of neodymia and gadolinia contents seem systematically too high compared with the initial composition of the powder. The stabilizer content in the matrix is slightly lower than (error levels are very high, 20 – 50 % owing to the low concentration) in the starting powder.

Table 1: Chemical composition in coarse grains and fine matrix grains of TZP sintered at 1250 °C measured with EDX.

Location	ZrO_2 [mol%]	Nd_2O_3 [mol%]	Gd_2O_3 [mol%]	Al_2O_3 [mol%]
Observed band	ZrL	NdL	GdL	AlK
Coarse grains	78.83 ± 0.83	14.86 ± 0.39	5.97 ± 0.37	0.35 ± 0.25
Fine grain matrix	90.14 ± 1.62	2.27 ± 0.5	1.19 ± 0.6	0.73 ± 0.33

Fig. 5 shows the density of TZP and ATZ material determined with the Archimedes method versus sintering temperature. The TZP shows an initial increase in density from 5.9 g/cm³ at 1200 °C to 6.12 – 6.15 g/cm³ at 1250 – 1350 °C. For ATZ a density of 5.68 g/cm³ can be expected based on the rule of mixture. The reason for the initial decline in density is not evident, for an explanation, results from phase analysis and microstructural examination need to be considered.

(2) Mechanical properties

Fig. 6 shows the Vickers hardness HV10 of TZP and ATZ at different sintering temperatures. Both curves show a maximum, which is shifted to a 50-K-higher sintering temperature for ATZ. Owing to the higher hardness of alumina (~ 20 GPa) compared to zirconia (12 GPa), a higher hardness (by ~ 1.6 GPa) can be expected for ATZ. This hardness difference is found at 1300 and 1350 °C. Deviations at lower sintering temperature may be caused by incomplete stabilizer distribution.

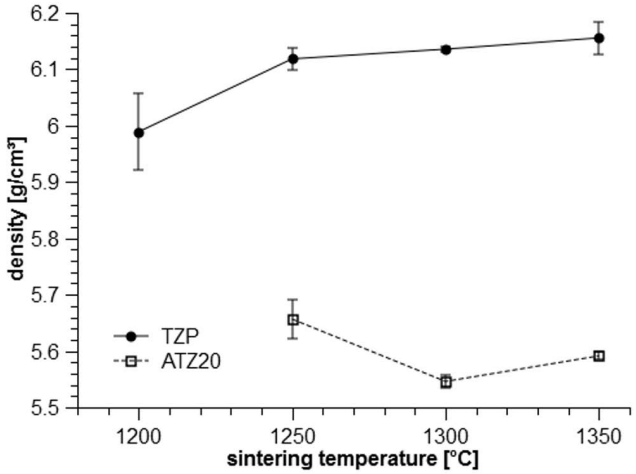

Fig. 5: Density of TZP and ATZ at different sintering temperatures.

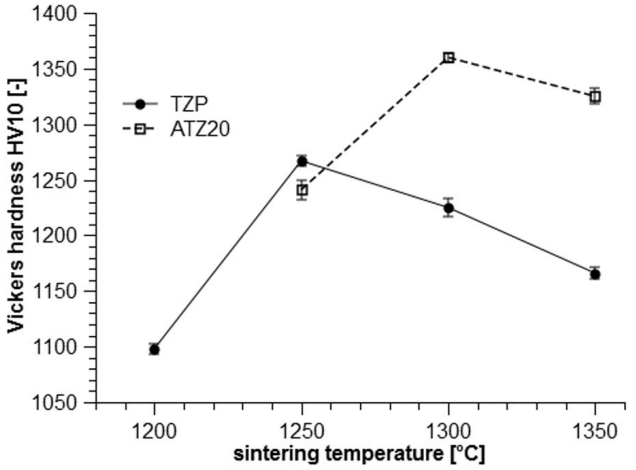

Fig. 6: Vickers hardness HV10 of TZP and ATZ vs. sintering temperature.

Fig. 7 shows the 4-pt-bending strength of TZP and ATZ versus sintering temperature. TZP shows an increase from 840 MPa at 1200 °C to 1080 MPa at 1350 °C. As expected, ATZ has higher strength than TZP. The highest strength of 1350 MPa for ATZ is observed at 1250 °C. At 1300 °C, a strength minimum occurs, then at 1350 °C strength rises again. The shape of the stress-strain curves (not shown) shows a shift from strictly linear elastic in the case of the materials sintered at 1200 – 1300 °C to non-linear elastic at higher sintering temperature. In the case of the materials sintered at 1350 °C, a decrease in the slope in the final stage of loading at > 800 MPa is observed. The indentation moduli determined by microindentation (not shown in detail) range between 218 GPa and 230 GPa for the TZP and between 248 GPa (1200 °C) and 272 GPa (1300 – 1350 °C) for ATZ. Fracture resistance values K_{IND} determined from crack length of HV10 indents (Anstis' model) and K_{ISB} measured with the residual strength method (ISB) are

displayed in Fig. 8. Except for the TZP sintered at 1200 °C, very high fracture resistance values of 8.5 – 11 MPa·√m (Anstis) and 10 – 15 MPa·√m (ISB) were observed. TZP shows higher fracture resistance than ATZ sintered at the same temperature irrespective of the measuring method. While the indentation fracture resistance profiles rise with the sintering temperature, the ISB tests show a toughness maximum for TZP at 1300 °C and a toughness minimum for ATZ at the same temperature. The toughness minimum for ATZ coincides with the strength minimum shown in Fig. 7. Besides the maximum toughness, the threshold stress intensity K_0 describing the resistance against sub-critical crack growth is highly interesting for engineering ceramics. Figs. 9 and 10 show the stress intensity versus crack extension curves of TZP and ATZ materials determined based on stable indentation crack growth in flexure. The TZP sintered at 1200 °C showed very inconsistent results and is therefore not shown. Evidently it is not possible to grow long cracks in TZP and even less so in the case of ATZ. The non-linearity of the curve, all curves tend to flatten with rising distance from the kink, indicates R-curve behaviour. The highest toughness values determined based on stable indentation crack growth in flexure are higher than measured by means of direct crack length measurement (K_{IND}). As the test is more or less identical with the ISB test except for the stepwise instead of continuous loading, similar maximum toughness is obtained as with ISB. It is quite obvious that a linear extrapolation with a constant slope would lead to unrealistically high toughness values. It was thus assumed that the intercept with the ordinate = K_{ISB} and that K_0 can be calculated from the difference K_{ISB}-$K_{App,0}$. The values determined with this procedure can be regarded as upper limits for K_0. A lower limit may be obtained by assuming that $K_0 = K_{IND} - K_{App,0}$. Indentation toughness K_{IND} according to Anstis is significantly lower and in most cases does not reach the highest value determined based on stable indentation crack growth in flexure. The threshold toughness values extracted from a plot of $\psi \cdot \sigma \sqrt{c}$ versus $P \cdot c^{-1.5}$ range from $K_0 = 5.6 - 7.6$ MPa·√m for the TZP and 3.6 – 5.7 MPa·√m for ATZ. As the results must be interpreted using different measurement protocols and as the number of data points collected is limited, the result inevitably has a high standard deviation totalling from the uncertainties in correct location of the kink and the standard deviation of the determination of K_{ISB}. Nevertheless, the data indicate that overall toughness is very high given the high strength and that the threshold stress intensity K_0 toughness is much higher compared to standard 3Y-TZP (~ 2.5 – 3.5 MPa·√m) [26].

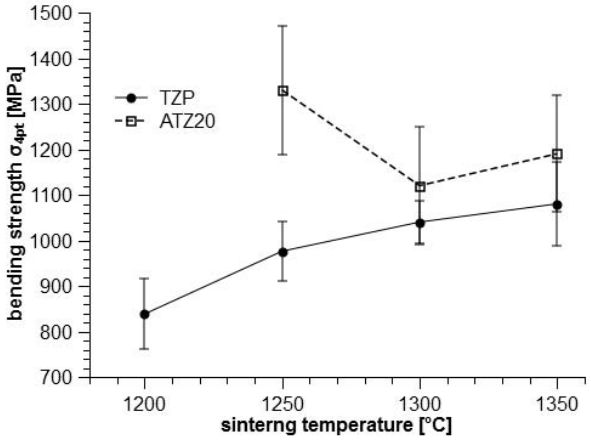

Fig. 7: Bending strength σ_{4pt} of TZP and ATZ vs. sintering temperature.

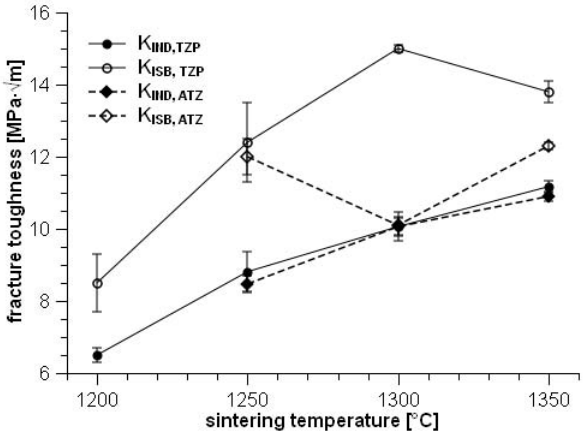

Fig. 8: Fracture resistance of TZP and ATZ vs. sintering temperature determined with direct crack length measurement and ISB method.

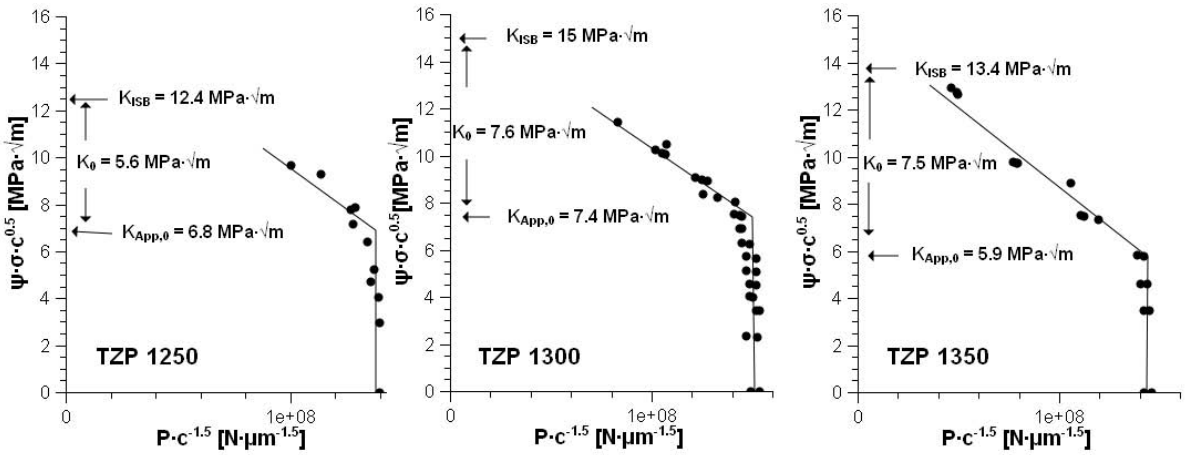

Fig. 9: Crack propagation curve of indentation cracks in TZP sintered at 1250 – 1350 °C representing the applied stress intensity factor versus $Pc^{-1.5}$ (P is the applied load and c is the crack length).

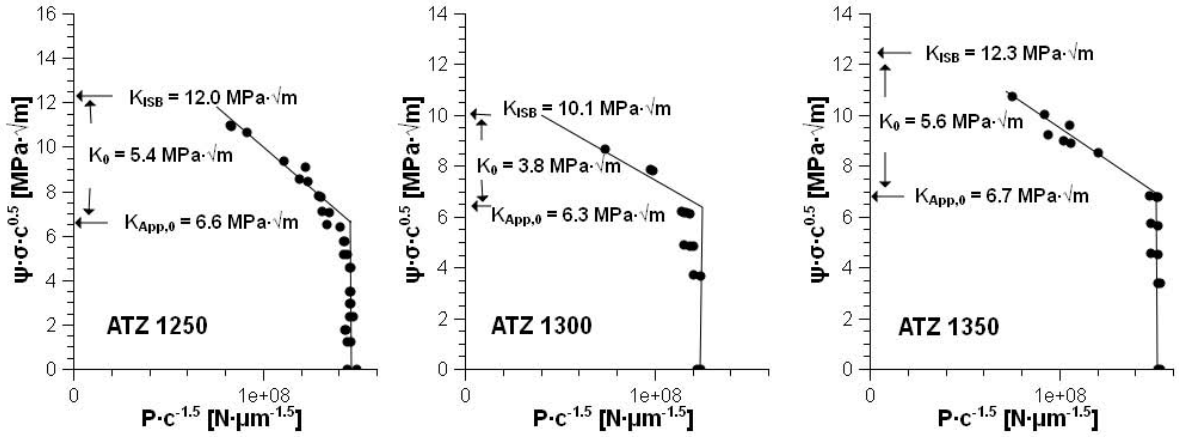

Fig. 10: Crack propagation curves of indentation cracks in ATZ sintered at 1250 – 1350 °C representing the applied stress intensity factor versus $Pc^{-1.5}$ (P is the applied load and c is the crack length).

(3) Phase analysis

Figs. 11 and 12 show the monoclinic content of zirconia in polished surfaces and fracture faces of TZP and ATZ. The difference between these two values is the transformability. In TZP the monoclinic content stays low (< 5 vol%) up to a sintering temperature of 1300 °C. At 1350 °C the monoclinic content rises to 30 vol%. At 1400 °C (this sample was broken to pieces and could not be further mechanically characterized) the monoclinic content rises to 70 %. In the case of ATZ, the monoclinic content is higher at 1250 °C (12 vol%) but rises only moderately to 18.5 vol% at 1350 °C.

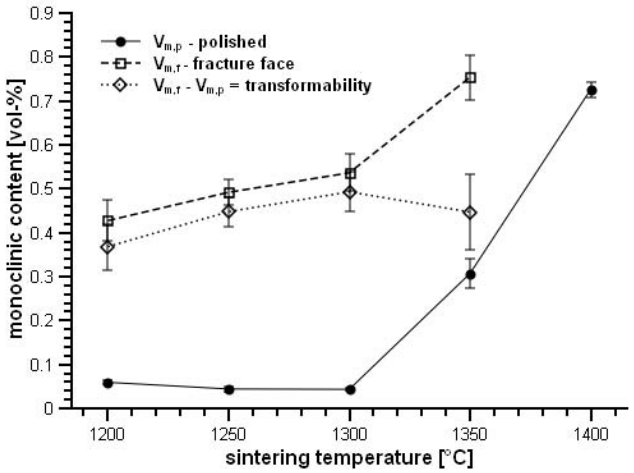

Fig. 11: Monoclinic content in polished surface and fracture faces of TZP.

A more detailed analysis shows that the tetragonal (101) reflex has a pronounced shoulder at the low 2θ edge which develops into a separate reflex (29.9° 2θ-scale) at higher sintering temperature (Fig. 13). Using a peak separation routine enables the integration of the two reflexes. Assuming that the zirconia content per area is identical to tetragonal, the additional phase would account for ~ 15 area% of zirconia in total at 1350 °C (Fig. 14). A study of the XRD patterns of fracture faces shows that while the tetragonal (101) reflex declines, the second peak at 29.9° remains unchanged (Fig. 15). The phase is obviously untransformable. EDX results have shown that large grains are enriched in stabilizer. Possible explanations are the presence of fluorite phase (cubic zirconia), orthorhombic or pyrochlore phase. In Y-TZP the $(111)_c$ reflex coincides with the $(101)_t$, thus presence of cubic is checked in the 2θ-range between 72 – 75°, here no cubic (400) reflex can be extracted from the background for any of the tested materials (Fig. 16). Cross checking with available results on zirconia neodymia compounds leads to a good match with JCPDS file 82 – 1015 describing a compound containing 38 – 41 mol% Nd_2O_3. The (111) reflex of cubic phase (fluorite structure)according to this reference appears at 29°. This also explains the absence of the cubic (400) reflex at 73.8°. The reflex is shifted to lower angles and coincides now with the $(004)_t$ reflex. Pyrochlore appears at lower 2θ only in compounds with significantly higher neodymia contents [30].

IV. Discussion

The TZP and ATZ materials produced exhibit extraordinarily high toughness despite their small grain size. Toughness rises with crack length, once the crack starts to grow, the crack propagation finishes after < 100 µm and the components finally fail. High strength of σ_{4pt} = 1000 – 1300 MPa combined with high toughness K_{ISB} of 10 – 15 MPa·√m and a very high threshold stress intensity K_0 of up to 5.5 – 7.6 MPa·√m are rare in the field of engineering ceramics. The best TZP materials known to date are Ce-TZP/alumina and Ce-TZP/spinel composites with σ_{4pt} ~ 900 MPa, K_{IC} = 8 – 15 MPa·√m and K_0 of 5 – 8 MPa·√m [27, 31]. At first sight, such property profiles seem somewhat contradictory to the accepted theory. The following considerations will show that there is no conflict.

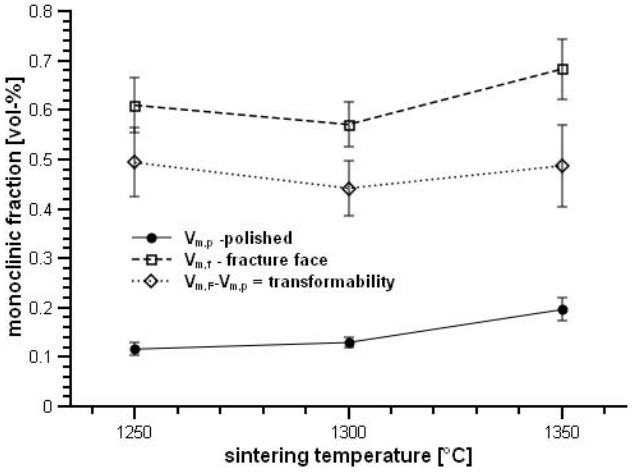

Fig. 12: Monoclinic content in polished surface and fracture faces of ATZ.

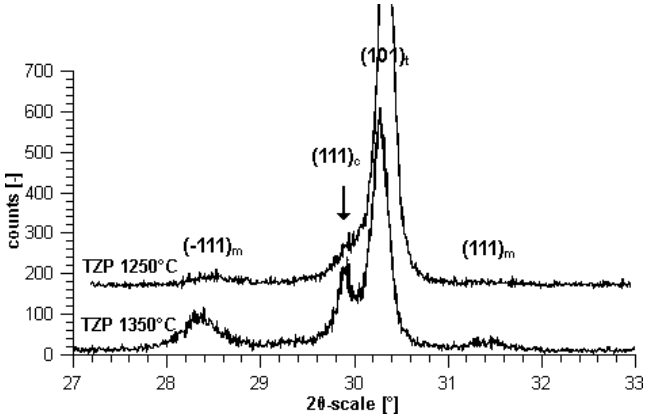

Fig. 13: XRD-diagram of the 27 – 33° 2θ-range of TZP sintered at 1250 °C and 1350 °C.

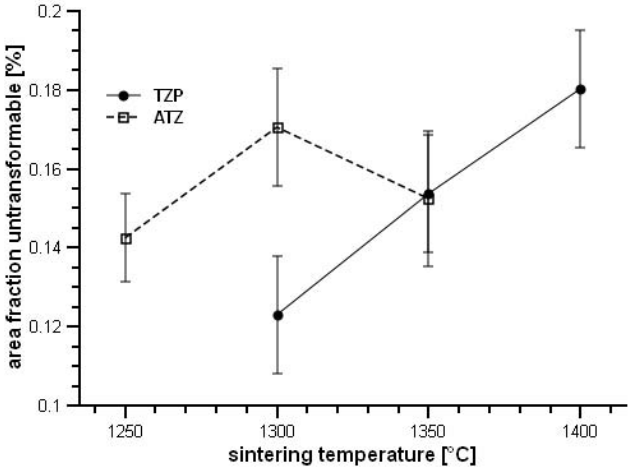

Fig. 14: Tentative calculation of volume fraction of untransformable phase in TZP and ATZ.

Very high strength and toughness in fine-grain TZP derived from coating processes have been reported before [7, 20]. Explanation models include effects like transformation toughening, microcracking and residual stress. The higher phase transformability compared to co-precipitated TZP is explained by either formation of a stabilizer gradient from grain boundary to bulk and or a broadening of the grain size distribution at higher sintering temperatures [7, 32, 33]. In the case of the composites, residual cooling stress introduced by the CTE difference of TZP and alumina further complicates the situation.

According to McMeeking and Evans, the transformation-derived toughness increment ΔK_C^T is: [34]

$$\Delta K_c^T = -\frac{X \cdot E \cdot V_f \cdot \varepsilon^T \cdot \sqrt{h}}{(1-\nu)} \qquad (2)$$

The parameters are: E = Young's modulus, V_f = transformed fraction, ε^T = transformation strain (0.05), h = half height of the transformed zone and ν = Poisson's ratio, the factor X in the original model is 0.22 for purely dilatant transformation. Including the shear component leads to an increase of X to 0.44 – 0.48 [35]. All variables except h were measured. The value for h can be measured with XRD or Raman spectroscopy or calculated using the following expression developed by Budianski [36]:

$$h = \frac{\sqrt{3} \cdot (1-\nu)^2}{12\pi} \cdot \left(\frac{K_\infty}{\sigma_c}\right)^2 \qquad (3)$$

In the present case of very high transformability it was considered that the calculation of h would be more reliable as the measurement with XRD must inevitably lead to values that are too low owing to the limited penetration depth of the X-rays [37]. *A priori* we may assume that the largest transformation zone height will develop under the condition that $K_\infty = K_{ISB}$ and σ_C = the bending strength required to induce critical crack growth. The latter was determined in the ISB measurements.

The comparison with experimentally determined values shows that transformation toughening is the dominant toughening mechanism.With calculated transformation zone sizes of h = 5.6 – 7.5 μm and a value of X = 0.27, transformation toughness increments ΔK_C^T of 4.5 – - 5.2 MPa·√m are obtained (Table 2) [38]. *A priori* the value X = 0.27 was chosen considering that the crystallographic boundary conditions of transformation for other trivalent rare earth dopants are probably similar to Y-TZP. Fracture resistance can be estimated by using a typical fracture resistance of the material in the transformation zone immediately ahead of the crack tip (K_{tip} = 4 MPa·√m as for Y-TZP). Assuming that $K_\infty = K_{tip} + \Delta K_C^T$ this would lead to fracture resistance values of 8.5 – 9.2 MPa·√m, these values are considerably lower than measured. It is thus quite likely that additional mechanisms such as microcracking do contribute to toughness. Microcracking was indicated in bending tests by the reduced slope in the final stage loading before fracture.

Another effect to be considered is a change in K_{tip} (not to be confused with K_0) induced by residual stress. As mentioned, the values for K_{tip} range between 3 – 4 MPa·√m for Y-TZP, Ce-TZP and Mg-PSZ. We may assume that these values are the "intrinsic" K_{tip} values [38]. Some indications of higher than usual K_{tip} values can be derived from numerical calculations by Amazigo and Budiansky. The relation between the toughness ratio K_{tip}/K_{IC} and

the normalized transformation strain is given by the term $((1+\nu)\cdot(E\cdot V_f\cdot\varepsilon^T))/((1-\nu)\cdot\sigma_C)$ [39].

With the experimentally determined values a normalized transformation strain of 10 – 20 for both TZP and ATZ can be calculated, this corresponds to a ratio of 0.3 – 0.6 for K_{tip}/K_{IC} (assuming that $K_{IC} = K_{ISB}$). Based on this calculation we can estimate an upper limit of K_{tip} of ~ 8 MPa·√m for TZP1300 and ~ 5.5 MPa·√m for ATZ1350. (Again: K_{tip} has nothing to do with K_0 even if the values are similar).

Table 2: Calculated transformation zone height and transformation toughness increments for TZP and ATZ.

	h [μm]	ΔK_C^T X =0.27 [MPa·√m]	$K_{ISB, exp.}$ [MPa·√m]
TZP1250	6.3	4.6	12.4
TZP1300	5.6	4.6	15
TZP1350	5.7	4.5	13.8
ATZ1250	6.8	4.8	12
ATZ1300	7.6	5	10.1
ATZ1350	6.6	5.2	12.3

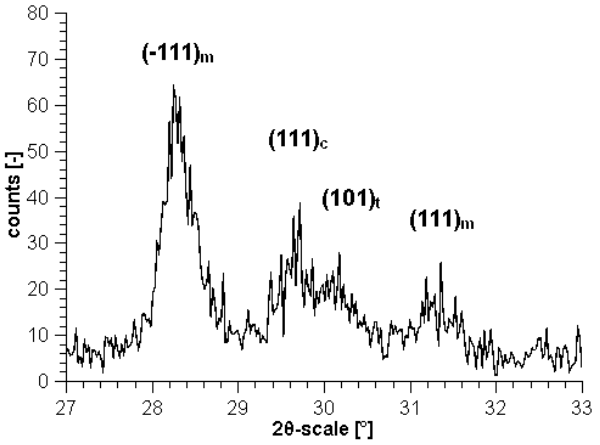

Fig. 15: XRD diagram of the 27 – 33° 2θ-range: fracture face of TZP sintered at 1300 °C.

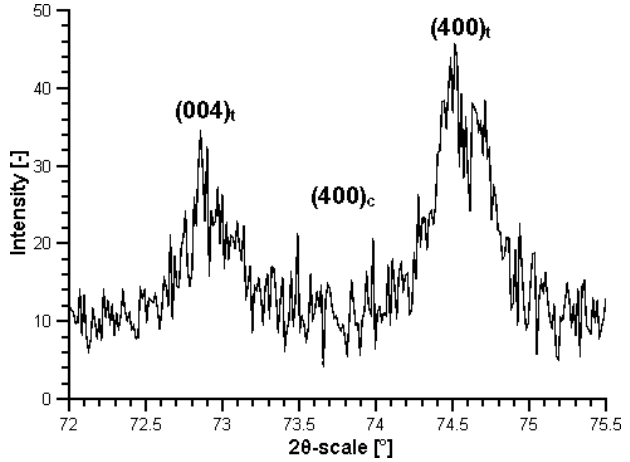

Fig. 16: XRD-diagram of the 72 – 75.5° 2θ-range of the polished surface of TZP sintered at 1300 °C.

Toughening effects taking place in the wake of the crack, like crack bridging, crack deflection, transformation or ferroelastic toughening and microcracking, cannot account for an increase of the fracture resistance ahead of the crack tip as they require crack extension. McMeeking and Evans have shown clearly that there is no net toughening in the cardioid transformation zone developing in front of the crack tip before crack extension starts. Hence there is no toughening until the crack starts to grow [34]. This has been confirmed by Budiansky based on a different approach [36].

In the present case (Figs. 11, 12) the materials always contain a certain fraction of monoclinic, which was formed from large transformable tetragonal grains during cooling. A fully tetragonal TZP can be considered macroscopically stress-free, at microscopic scale, stress is present owing to the inclination of grains with different crystallographic orientations. In ATZ during cooling from sintering temperature the thermal mismatch between alumina and zirconia generates compressive cooling stress in alumina and tensile stress in zirconia.

Formation of monoclinic accompanied by volume expansion will set the surrounding TZP matrix under compression and compensate the tensile stress induced by alumina in ATZ. Residual compressive stress in the TZP matrix can be superimposed to applied stress inhibiting crack opening.

A similar effect is purposefully produced by surface grinding of transformation-toughened materials to introduce compressive stress [40]. In the present case a machining-induced phase transformation can be ruled out as the machining was performed very gently without grinding operation. Compressive stress in coated Y-TZP has been verified by Ohnishi [7]. As shown in Eq. (2), the fracture toughness derived from transformation is proportional to the product of the square root of transformation depth √h and transformed fraction V_f. Mori has investigated this relationship in detail for co-precipitated Y-TZP and found a linear correlation irrespective of stabilizer content [41]. Ohnishi has shown the relations for 2 – 3.5Y-TZP obtained with a coating process. He found high toughness at much lower $V_f\sqrt{h}$ values than in co-precipitated TZP and that relations vary with yttria content [42]. Fig. 17 shows such a plot for GdNd2-TZP and ATZ. For the ATZ, the transformed fraction from Fig. 12 was multiplied by the volume fraction of zirconia (0.8), the value for h was calculated with Eq. 3. Both data sets – with a quite large scatter – fit into the same rising trend, a drop as reported by Ohnishi for 2Y-TZP and 2.5 Y-TZP was not observed.

However, the data points of the present study cover too narrow a range to be able to give a clear statement at this point. The GdNd2-TZP and ATZ show similar values for $V_f\sqrt{h}$ as in 2.5 – 2.8 Y-TZP studied by Ohnishi but considerably higher toughness [7].

The effect of alumina addition to co-precipitated TZP has been discussed by Swain in terms of a reduction of critical flaw size causing an increase in strength [38]. At the prevailing high level of toughness, processing-related flaws of 3 – 10 μm size which are typical for high-quality engineering ceramics are not critical at the level of toughness and

final strength observed. Still the ATZ materials have higher strength as they are not as tough and thus less R-curve dominated than the TZPs.

An interesting point is the shift in monoclinic content in as-fired state caused by alumina addition. Originally, alumina was added to Y-TZP not only to increase the strength but also to improve the aging resistance. Ross has shown in TEM studies that alumina is incorporated in the first few atomic layers at the grain boundary of TZP [42]. The half percent of alumina in the TZP should be sufficient to ensure increased stability compared to plain TZP. Alumina added to TZP creates tensile residual cooling stress in the TZP matrix, making it more transformable. Gregori has calculated that the stress-neutral state in ZTA is at ~ 20 vol% monoclinic, this level is composition-independent but may vary with sintering temperature [43]. For an ATZ containing 20 vol% alumina and entirely tetragonal zirconia, the TZP matrix is under a tensile stress of 80 – 100 MPa [44]. The residual stresses are proportional to $\Delta\alpha\Delta T$, the product of CTE difference and the difference of ambient and processing temperature. In the case of ATZ sintered at a lower temperature than ZTA (1450 °C), we may expect the stress-neutral state at 15 – 20 vol% monoclinic. In the present case the TZP is the matrix and not the dispersion so that partial accommodation of these stresses may occur during cooling as a result of creep. Evidently the residual stress introduced by alumina is high enough to trigger monoclinic phase formation in the highly transformable grains of the GdNd2-TZP matrix. The higher monoclinic content observed in ATZ is thus in line with predictions. Monoclinic fraction in ATZ rises moderately and alumina stabilizes the phase composition at high sintering temperature. Comparing the results of the present study with the limits of strength-toughness correlations defined by Swain for transformation-toughened alloys, it is observed that the measured values are at or beyond the defined limits [38]. A brief look at the database used shows that, as a rule of the thumb, zirconia materials become R-curve dominated at a K_{IC} of ~ 8 MPa·√m or (given that K_{tip} = 4 MPa·√m) in other terms at K_{IC} - K_{tip} = ΔK_C > 4 MPa·√m. This prerequisite is fulfilled (see Table 2). The restrictions defined by Swain are, however, only valid for toughening processes in the wake or process zone. Thus a higher fracture resistance before the crack tip can shift the strength limits to higher values so that materials with higher strength can be obtained at identical toughness (or vice versa).

Concerning the composition of the untransformable phase, the following interpretation can be given. The additional reflex is caused by a cubic-stabilizer-rich zirconia compound with fluorite structure, the corresponding reflex can be clearly identified [30]. Co-precipitated 3Y-TZP with an initially homogeneous stabilizer distribution is quite inert against phase separation. Matsui has shown that phase separation in the t+c field proceeds quite slowly and requires high temperatures or very long dwell [45]. In GdNd2-TZP and ATZ derived from stabilizer-coated powder the t+c field represents is a real miscibility gap in which phase separation proceeds at low temperature and short dwell. Different to Y-TZP, the phase separation seems to include the whole grains, no indications were found that the cubic formation starts in localized areas within grains. The initial non-uniformity of stabilizer distribution in the coated powder may assist this separation process. According to Wang the solubility limit of Nd_2O_3 ranges between 1 – 1.2 mol% at firing temperature, the invariant reaction T → M+P occurs at 1326 °C and 0.5 mol% Nd_2O_3. The TZP is thus supersaturated with neodymia, in the case of gadolinia the same holds true, the invariant reaction T → M+F occurs at 1309 °C and 0.7 mol% Gd_2O_3 [13]. The separation of a cubic phase is thus thermodynamically favoured.

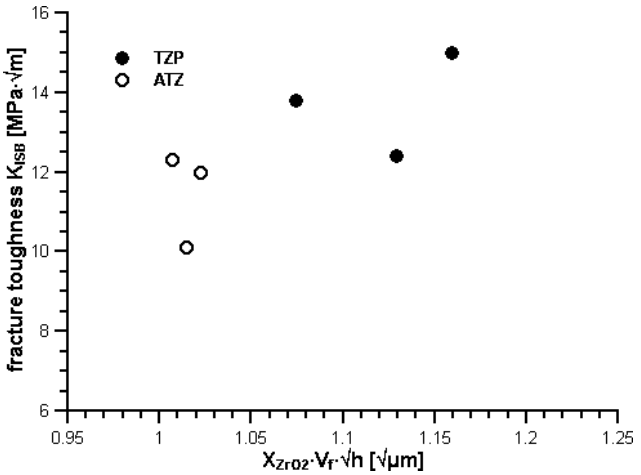

Fig. 17: Relation between the product of transformation depth and transformed fraction and fracture toughness.

V. Conclusion

GdNd2-TZP and ATZ produced from unstabilized nanopowder via the nitrate route exhibit a bimodal microstructure with a fraction of large untransformable cubic grains embedded in an extremely fine tetragonal zirconia matrix. Both materials exhibit a combination of high toughness and high strength. Threshold stress intensity is very high and reaches levels of 5.5 – 7.5 MPa·√m. The calculated transformation toughness increments amount to 4 – 5 MPa·√m. The transformability of the tetragonal phase in both TZP and ATZ is high (44 – 50 %). Crack extension is small but process zones are larger than in 3Y-TZP. Crack deflection or microcracking may provide a further toughening increment of up to 2 MPa·√m in TZP especially at higher sintering temperatures.

Thanks to their strength, toughness and threshold stress intensity, the materials developed are very interesting structural ceramics. Especially the high threshold K_0 is attractive for cyclically loaded components. The extreme reliability and flaw insensitivity of the co-stabilized materials may offer new perspectives in ceramics manufacturing. A more detailed investigation of coated TZP materials with different stabilizers and stabilizer concentrations will be necessary to validate the assumptions made. The results shown may lead to a different approach in tailoring high-toughness TZP materials with a focus on optimizing threshold stress intensity and not only the transformation-related increment.

References

1 Kelly, P.M., Rose, L.R.F.: The martensitic transformation in ceramics – its role in transformation toughening, *Prog. Mat. Sci.*, **47**, 463 – 557, (2002).

2 Hannink, R.J., Kelly, P.M., Muddle, B.C.: Transformation toughening in zirconia-containing ceramics, *J. Am. Ceram. Soc.*, **83**, [3], 461 – 87, (2000).

3 Grathwohl, G., Liu, T.: Crack resistance and fatigue of transforming Ceramics: II, CeO_2-stabilized tetragonal ZrO_2, *J. Am. Ceram. Soc.*, **74**, [12], 3028 – 34, (1991).

4 Grathwohl, G., Liu, T.: Crack resistance and fatigue of transforming Ceramics: I, materials in the ZrO_2-Y_2O_3-Al_2O_3 system, *J. Am. Ceram. Soc.*, **74**, [2], 318 – 25, (1991).

5 Tsukidate, T., Tsukuma, K.: Partially stabilized zirconia powder, *Ceram. Jpn.*, **17**, 816 – 822, (1982).

6 Yuan, Z.X., Vleugels, J., Van der Biest, O.: Preparation of Y_2O_3-coated ZrO_2 powder by suspension drying, *J. Mat. Sci. Let.*, **19**, 359 – 361, (2000).

7 Ohnishi, H., Naka, H., Sekino, T., Ikuhara, Y., Niihara, K: Mechanical properties of 2.0 – 3.5 mol% Y_2O_3-stabilized zirconia polycrystals fabricated by the solid phase mixing and sintering method, *J. Ceram. Soc. Jap.*, **116**, 1360, 1270 – 1277, (2008).

8 Kern, F: Alumina-doped 2.5Y-TZP produced from yttria-coated pyrogenic nanopowder, *J. Ceram. Sci. Tech.*, **2**, [2], 89 – 96, (2011).

9 Picconi, C., Burger, W., Richter, H.G., Cittadini, A., Maccauro, G., Covacci, V., Bruzzese, N., Ricci, G.A., Marmo, E.: Y-TZP ceramics for artificial joint replacements, *Biomaterials*, **19**, 1489 – 1494, (1998).

10 Kan, Y., Li, S., Wang, P., Zhang, G., Van der Biest, O., Vleugels, J.: Preparation and conductivity of Yb_2O_3-Y_2O_3 and Gd_2O_3-Y_2O_3 co-doped zirconia ceramics, *Solid State Ionics*, **179**, 1531 – 1534, (2004).

11 Huang, S., Li, L., Van der Biest, O., Vleugels, J.: Microwave sintering of CeO_2 and Y_2O_3 co-stabilised ZrO_2 from stabiliser-coated nanopowders, *J. Eur. Ceram. Soc.*, **2**, 7 689 – 693, (2007).

12 Vleugels, J., Xu, T., Huang, S., Kan, Y., Wang, P., Li, L., Van der Biest, O.: Characterization of (Nd,Y)-TZP ceramics prepared by a colloidal suspension coating technique, *J. Eur. Ceram. Soc.*, **27**, 1339 – 43, (2007).

13 Wang, C., Zinkevich, M., Aldinger, F.: Phase diagrams and thermodynamics of rare-earth-doped zirconia ceramics, *Pure Appl. Chem.*, **79**, [10], 1731 – 1753, (2007).

14 Andrievskaya, E.R., Lopato, L.M.: Influence of composition on the T- M transformation in the systems ZrO_2-Ln_2O_3 (Ln = la, nd, sm, Eu), *J. Mater. Sci.*, **311**, 2591 – 2596, (1995).

15 Rouanet, A.: Contribution to study of zirconium-oxides systems of lanthanides close to the melting point, *Rev. Int. Haut. Temp. Refract.*, **8**, [2], 161 – 180, (1971).

16 Hinatsu, Y., Muromura, T.: Phase relations in the systems ZrO_2-Y_2O_3-Nd_2O_3 and ZrO_2-Y_2O_3-CeO_2, *Mat. Res. Bull.*, **21**, [11], (2003).

17 Lakiza, S., Fabrichnaya, O., Wang, C., Zinkevich, M., Aldinger, F.: Phase diagram of the ZrO_2-Gd_2O_3-Al_2O_3 system, *J. Eur. Ceram. Soc.*, **26**, 233 – 246, (2006).

18 Salehi, S., Van der Biest, O., Vleugels, J.: Y_2O_3 and Nd_2O_3 Co-stabilized ZrO_2-WC composites, *J. Mater. Sci.*, **43**, 5784 – 5789, (2008).

19 Salehi, S., Yüksel, B., Vanmeensel, K., Van der Biest, O., Vleugels, J.: Y_2O_3-Nd_2O_3 double stabilized ZrO_2-TiCN nanocomposites, *Mater. Chem. Phys.*, **113**, 596 – 601, (2009).

20 Gadow, R., Kern, F.: Novel zirconia-alumina nanocomposites combining high strength and toughness, *Adv. Eng. Mat.*, **12**, [12], 1220 – 1223, (2010).

21 Quinn, G., Bradt, R.: On the vickers indentation fracture toughness test, *J. Am. Ceram. Soc.*, **90**, [3], 673 – 680, (2007).

22 Krell, A.: Features of notch preparation for fracture toughness measurements in partially stabilized zirconia, *J. Am. Ceram. Soc.*, **77**, [2], 600 – 602, (1994).

23 Kern, F., Gadow, R.: Ytterbia (2.25 mol.-%) stabilised zirconia (Yb-TZP) manufactured from coated nanopowder, *Adv. Appl. Ceram.*, DOI: 10.1179/1743676111Y.0000000071, (2012).

24 Anstis, G.R., Chantikul, P., Lawn, B.R., Marshall, D.B.: A critical evaluation of indentation techniques for measuring fracture Toughness: I, direct crack measurements, *J. Am. Ceram. Soc.*, **64**, [9], 533 – 538, (1981).

25 Chantikul, P., Anstis, G.R., Lawn, B.R., Marshall, D.B.: A critical evaluation of indentation techniques for measuring fracture Toughness: II, strength method, *J. Am. Ceram. Soc.*, **64**, [9], 539 – 543, (1981).

26 Dransmann, G., Steinbrech, R., Pajares, A., Guiberteau, F., Dominguez-Rodriguez, A., Heuer, A.: Indentation studies on Y_2O_3,-stabilized ZrO_2: II, toughness determination from stable growth of indentation-induced cracks, *J. Am. Ceram. Soc.*, **77**, [5], 1194 – 201, (1994).

27 Benzaid, R., Chevalier, J., Saadaoui, M., Fantozzi, G., Nawa, M., Diaz, L.A., Torrecillas, R.: Fracture toughness, strength and slow crack growth in a ceria stabilized Zirconia-Alumina nanocomposite for medical applications, *Biomaterials*, **29**, 3636 – 3641, (2008).

28 Lube, T., Fett, T: A threshold stress intensity factor at the onset of stable crack extension of knoop indentation cracks, *Eng. Fract. Mech.*, **71**, 2263 – 2269, (2004).

29 Toraya, H., Yoshimura, M., Somiya, S.: Calibration curve for quantitative analysis of the monoclinic-tetragonal ZrO_2 system by X-ray diffraction, *J. Am. Ceram. Soc.*, **67**, [6], C119 – 121, (1984).

30 Liu, Z., Ouyang, Z., Zhou, Y., Li, J.: Effect of alumina addition on the phase evolution and thermal conductivity of ZrO_2-$NdO_{1.5}$ ceramics, *J. Alloys Comp.*, **468**, 350 – 355, (2009).

31 Apel, E., Ritzberger, C., Courtois, N., Reveron, H. *et al.* : Introduction to a tough, strong and stable Ce-TZP/$MgAl_2O_4$ composite for biomedical applications, *J. Eur. Ceram. Soc.*, doi:10.1016/j.jeurceramsoc.2012.02.002, (2012).

32 Vleugels, J., Yuan, Z., Van Der Biest, O.: Mechanical properties of Y_2O_3/Al_2O_3-coated Y-TZP ceramics, *J. Eur. Ceram. Soc.*, **22**, 873 – 881, (2002).

33 Burger, W., Richter, H.G., Piconi, C., Zatteroni, R., Cittadini, A., Boccalari, M.: New Y-TZP powders for medical grade zirconia, *J. Mater. Sci., Mater. M.*, **8**, 113 – 118, (1997).

34 McMeeking, R., Evans, A.G.: Mechanics of transformation-toughening in brittle materials, *J. Am. Ceram. Soc.*, **65**, [5], 242 – 246, (1982).

35 Chen, I.W., Reyes-Morel, P.E.: Implications of transformation plasticity in ZrO_2-containing Ceramics: I, shear and dilatation effects, *J. Am. Ceram. Soc.*, **69**, [3], 181 – 189, (1986).

36 Budiansky, B., Hutchinson, J.W., Lambropolous, J.C.: Continuum theory of dilatant transformation toughening in ceramics, *Int. J. Solids Struct.*, **19**, [4], 337 – 55, (1983).

37 Kosmac, T., Wagner, R., Claussen, N.: X-ray determination of transformation depths in ceramics containing tetragonal ZrO_2, *J. Am. Ceram. Soc.*, **64**, [4], C72 – 73, (1981).

38 Swain, M.V., Rose, L.R.F.: Strength limitations in transformation-toughened zirconia alloys, *J. Am. Ceram. Soc.*, **69**, [7], 511 – 18, (1986).

39 Amazigo, J., Budiansky, B.: Interaction of particulate and transformation toughening, *J. Mech. Phys. Solids*, **36**, [5], 581 – 595, (1988).

40 Xu, H., Jahanmir, S., Ives, L.: Effect of grinding on strength of tetragonal zirconia and zirconia toughened alumina, *Machining Sci. Techn.*, **1**, [1], 49 – 66, (1997).

[41] Mori, Y., Kitano, Y., Ishitani, A., Masaki, T.: X-ray determination of transformation zone size in toughened zirconia ceramics, *J. Am. Ceram. Soc.*, **71**, [7], C-322-C-324, (1988).

[42] Ross, I.M., Rainforth, W.M., Comb, D.W., Scott, A.J., Brydson, R.: The role of trace additions of alumina to yttria-tetragonal zirconia polycrystals (Y-TZP), *Scripta Mater.*, **45**, 653 – 660, (2001).

[43] Gregori, G., Burger, W., Sergo, V.: Piezo-spectroscopic analysis of the residual stresses in zirconia-toughened alumina Ceramics: the influence of the tetragonal-to-monoclinic transformation, *Mater. Sci. Eng.*, **A271**, 401 – 406, (1999).

[44] Kern, F., Gadow, R.: Alumina toughened zirconia from yttria coated powders, *J. Eur. Ceram. Soc.*, doi:10.1016/j.jeurceramsoc.2012.03.014, (2012).

[45] Matsui, K., Horikoshi, H., Ohmichi, N., Ohgai, M., Yoshida, H., Ikuhara, Y.: Cubic-formation and grain-growth mechanisms in tetragonal zirconia polycrystal, *J. Am. Ceram. Soc.*, **86**, [8], 1401 – 1408, (2003).